Journal of Minerals and Materials Characterization and Engineering, 2024, 12, 299-315
https://www.scirp.org/journal/jmmce
ISSN Online: 2327-4085
ISSN Print: 2327-4077

Portevin-Le Chatelier Effect in Additively Manufactured and As-Cast Inconel 939 Nickel-Based Superalloy

Moshe Nahmany[1,2], Daniel Moreno[1*], Yohanan Nahmana[1], Mathan Zakai[1], Ariel Yehuda Cohen[1], Moshe Shapira[1], Roni Shneck[3]

[1]Bet Shemesh Engines Ltd., FAA&EASA, Bet Shemesh, Israel
[2]Nuclear Research Center-Negev, Beer Sheva, Israel
[3]Department of Materials Science and Engineering, Ben-Gurion University of the Negev, Beer Sheva, Israel
Email: *danielm@bsel.co.il

How to cite this paper: Nahmany, M., Moreno, D., Nahmana, Y., Zakai, M., Cohen, A.Y., Shapira, M. and Shneck, R. (2024) Portevin-Le Chatelier Effect in Additively Manufactured and As-Cast Inconel 939 Nickel-Based Superalloy. *Journal of Minerals and Materials Characterization and Engineering*, **12**, 299-315.
https://doi.org/10.4236/jmmce.2024.126019

Received: September 1, 2024
Accepted: November 1, 2024
Published: November 4, 2024

Abstract

Nickel-based superalloys, well-established in aeronautics, have recently gained significant traction in additive manufacturing. Inconel 939 is one of the alloys increasingly playing a vital role in this field. This paper examines the development of the Portevin-Le Chatelier (PLC) effect in additively manufactured Inconel 939 in comparison with cast Inconel 939. A detailed analysis of tensile test characteristics was conducted, complemented by a high-resolution scanning electron microscopy (HR-SEM) investigation. The PLC region exhibited several properties during tensile testing, such as stress-strain behavior, cycle scale, and overall stress increase. The HR-SEM analysis of Gamma prime (γ') precipitates revealed distinct morphologies, which are suggested to be linked to the features of the PLC region. Samples with a high amount of γ' precipitates showed a less pronounced PLC region, while those with fewer γ' precipitates displayed a more distinct PLC effect. A mechanism for the cyclic drop-and-rise stress behavior, based on the work of Varvenne and La-Rose, was proposed, possibly induced by the varying morphologies of γ' precipitates in the IN939 alloy. Further study is needed to deepen the understanding of the relationship between the γ' micro-(nano) structure and the PLC phenomenon.

Keywords

Inconel 939, Gamma Prime, γ', Portevin-Le Chatelier (PLC), Dynamic Strain Aging, DSA, Mechanical Properties, Additive Manufacturing, Superalloys

1. Introduction

Cast high-chromium Inconel 939 (IN939) alloy is widely utilized in industrial gas

turbines as a structural material exposed to moderate and high temperatures. Applications in aerospace engines, energy industries, the process industry, oil, gas, and shipbuilding, where exceptional oxidation resistance and high creep strength at elevated temperatures are essential, also use cast IN939. IN939 is a precipitation-hardened nickel-based superalloy, primarily employed over the last few decades for manufacturing high-temperature cast components, such as gas turbine blades and vanes, fuel nozzles, and turbine castings [1] [2]. This promising cast alloy is employed in combustion turbines up to 850˚C. However, the necessary joining technology for large structural components in aero engines poses a challenge, as investigated elsewhere [2].

The relatively recent additive manufacturing (AM) technology of Ni-based superalloys addresses serious problems and optimizes the complexity of engineered parts while reducing product development and marketing times. Despite the advantages of the AM technology, unacceptable defects, such as micro-cracks in the bulk and surface oxidation, were observed during production, degrading the mechanical properties of the alloy at high temperatures. Tolerances of composite elements, particularly Zr and B, influence the occurrence of micro-cracks [3]. Moreover, anisotropy was identified in the mechanical properties of (additively manufactured) AMed samples, owing to the layer deposition during manufacturing, the thermal process, and the solidification front. Those, in turn, are affecting the microstructure and, consequently, the failure modes [4].

The key property of a superalloy in a combustion turbine is high-temperature creep resistance. A recent study compares different heat treatments on IN939 [5]. A lower-temperature heat treatment (1160˚C/4 h + aging at 850˚C/16 h) resulted in small, recrystallized grains formed between the columnar grains; consequently, rupture elongation was large, but the creep life was poor due to harmful phases like η. In contrast, a higher-temperature heat treatment (solution at 1240˚C/6 h + aging at 850˚C/16 h) exhibited a creep life 2.7 times longer, due to full recrystallization and an increase in γ precipitate size during creep, albeit with very poor ductility [5]. Recently, it was observed that the precipitate, γ', in cast or wrought IN939 Superalloy, grows under low-cycle fatigue (LSW) at a temperature range of 790˚C - 910˚C for up to 1500 h, and the volume diffusion of alloying elements controls the growth rate [6].

Metallurgical microstructures obtained after AM processing differ from those obtained after conventional processing and affect high-temperature mechanical properties. Inconel 939, processed by selective laser melting (SLM), was examined, revealing influences of heat flux during layer-wise deposition and anisotropy in the microstructure [7]. Liquation cracking and strain age cracking in the heat-affected zone (HAZ) were characterized in welded IN939 and healed by hot isostatic pressing (HIP) [8]. Post-weld HIP was deemed necessary to obtain crack-free joints, although non-desirable new phases could be created during this thermodynamic process.

Non-conventional heat treatments were studied by Gonzalez *et al.* [9] as

alternative methods to restore the microstructure of long-term exposed blades to normal working conditions. Conventional two-stage heat treatment presented a lower volume fraction of primary γ' and coarse secondary γ', potentially affecting short-term tensile strength, whereas alternative heat treatments restored the microstructure. The sources cited in this introduction highlight the capacity of thermodynamic processes to improve the mechanical properties of the alloy through the microstructures obtained by different heat treatments [9]. Marchese *et al.* [10] investigated the microstructure and cracking mechanisms of laser powder bed fusion (LPBF) IN939, concluding that high thermal residual stresses obtained by rapid cooling and heating rates, along with the presence of intergranular precipitates, could be the causes of cracks along grain boundaries. Additionally, the reduction of powder could avoid intergranular carbides and cracks. Their work also suggests that HIP can effectively consolidate micro-cracks, reduce nominal porosity, and improve the mechanical properties of the material [10]. In materials science and engineering, the stress-strain test is a fundamental method used to characterize the mechanical properties of materials. When a material is subjected to increasing stress, its response is typically measured in terms of strain, which represents the amount of deformation experienced by the material. Close to the yield stress, where the material begins to exhibit plastic deformation, various phenomena may occur, including what is termed "unstable flow". Unstable flow refers to a set of plastic instabilities that arise during mechanical testing, leading to non-monotonic stress-strain behavior and the localization of strain. This means that instead of a smooth, continuous increase in strain with increasing stress, there are fluctuations and irregularities in the stress-strain curve. In constant strain rate tensile tests, a specific phenomenon of unstable flow is observed, known as the PLC effect. Lüders band and PLC bands can be explained by the difference between static strain aging (SSA) and dynamic strain aging (DSA). The dynamic strain aging effect is characterized by repeated load drops on the stress-strain curve. It was named after the individuals who made the first systematic observations of this phenomenon: Le Chatelier in steels [11] [12] and later in Al-Mg alloys [13]. In addition, modeling of PLC effects in Al alloys was performed and reported [14].

The objective of the present study is to report the fluctuations in stress and strain behavior of the Stress-Strain curve attributed to the PLC effect. The phenomenon has significant implications for understanding the mechanical behavior and performance of materials, particularly in high-stress or high-strain conditions in Ni-base superalloy.

2. Experimental

A high-powered EOS M400 Yb-fiber laser, boasting a beam spot quality of 1000 W, a speed of up to seven meters per second, excellent resolution, and precision, was employed in the current study for the fabrication of AMed samples. The IN939 powder, with a spherical shape and a general particle size ranging from 20 to 55 μm, along with its analyzed chemical composition (as detailed in **Table 1**),

Table 1. Alloy composition.

Sample/Elements (wt %)	Ni	Cr	Co	W	Al	Ta	Nb	Ti	Zr	C	B	Traces
Atomic Radius (Å)	1.25	1.25	1.25	1.37	1.43	1.49	1.43	1.45	1.59	0.71		
Commercial Powder Alloy EOS 9011-0030	Bal.	22.6	19.9	2.06	1.9	1.49	0.98	3.6	0.03	0.15	0.02	Si 0.2 max Others < 100 ppm
As cast	Bal.	22.8	19.5	1.9	1.9	1.35	0.9	3.6	0.02	0.16	0.004	Ag, Bi, Pb, Se, S, O, N
Ingot Alloy Standard	Bal.	22 - 22.8	18 - 19.5	1.8 - 2.2	1.8 - 2	1.3 - 1.5	0.9 - 1.1	3.6 - 3.8	0.02 - 0.03	0.13 - 0.17	0.004 - 0.006	Ag, Bi, Pb, Se, S, O, N

served as the primary material. The AMed samples were built in perpendicular orientation to the beam in two directions—X and Y, and parallel to the beam—Z direction.

Cylindrical rod samples derived from the prints underwent a specific heat treatment regime:

1) Solution treatment (Cycle 1): soak at 1190˚C for 4 hours, followed by rapid argon cooling to 30˚C - 40˚C.

2) Aging treatment (Cycle 2): soak at 1000˚C for 6 hours, followed by rapid argon cooling to 30˚C - 40˚C.

3) Aging treatment (Cycle 3): soak at 800˚C for 4 hours, followed by rapid argon cooling to room temperature.

Table 1 displays the analyzed chemical composition of the IN939 powder used in the study and some relevant metallurgical data.

Following heat treatment, the specimens were machined to form cylindrical ("dog-bone") mechanical property samples with the following dimensions: 6 mm in diameter, 24 mm gauge length (4D), and a total length of 75 mm. Flat samples, measuring 110 mm × 10 mm × 2 mm with a 25 mm gauge length, were machined as well, to 6 mm width at gauge. Tensile tests were conducted using a universal tensile machine at room temperature. The stress-strain curve was utilized in strain control mode at a rate of 0.50% per minute (up to 1.2% strain - until reaching the extensometer full scale) and then switched to crosshead control at 1.60 and 3.00 mm/min (flat and cylindrical respectively) up to failure. HR-SEM characterization was conducted using Verios 460L FEI SEM.

3. Results

Mechanical tensile Properties of AMed and casted reference IN939 at room temperature are presented in Table 2. The periodic trend times, as the time of the "PLC cycle", are shown along with the amplitudes of the PLC's serrations.

The AMed samples exhibit significantly higher ultimate tensile strength (UTS) and yield strength (YS) than cast IN939, with increases of 55% and ~41%, respectively (see Table 2 for the cylindrical specimens). Additionally, the elongation of the AMed specimens is approximately 2.5 to 3 times greater. An analysis of certain

Table 2. Mechanical properties of IN939 were obtained by analyzing the stress-strain and stress-time curves. AMed sample nomenclature denotes: C: cylindric samples; R: rectangular samples. Built directions: X, Y: perpendicular to the beam; Z: parallel to the beam. Calc.: calculated value; Est.: estimated value. The total rise in PLC for the cylindrical samples was derived from the main-steady PLC region.

Sample No.	UTS (MPa)	YS (MPa)	Elongation (%)	Young's Modulus (GPa)	PLC Δ Serrated Drop [MPa]	PLC cycle time [sec]	Total rise in PLC [MPa]	Rem.
1.1C.Z	1500	1070	15	196	36 - 40	3.85	22	Cal.
1.2C.Z	1510	1080	13	204	36 - 40	3.75	26	Cal.
2.1C.X	1530	1070	10	203	35 - 46	3.71	39	Cal.
2.2C.X	1560	1100	11	215	39 - 47	3.72	33	Cal.
3.1C.X	1550	1100	11	215	44			Est.
3.2C.X.	1550	1120	10	221	44			Est.
4.1C.Y	1550	1090	12	213	40			Est.
5.1C.Z	1490	1040	13	200	40			Est.
5.2C.Z	1490	1050	15	199	40			Est.
6.1R.Z	1270	995	7	195	2.6 - 5.8	2.1	42	Cal.
6.2R.Z	1240	985	7	204	3.5 - 7	2.1	41	Cal.
7.1R.X	1260	975	6.5	230	5 - 20	3	59	Cal.
7.2R.X	1270	980	6	224	5 - 14	3.2	57	Cal.
Cast (C)	965	765	4.5	232	63 - 78	3.7	69	Cal.

PLC characteristics showed some variations and anisotropy, particularly influenced by the build direction.

The Z-built samples demonstrated a lower total rise through the PLC region, averaging 24 MPa and 42 MPa for the cylindrical and rectangular specimens, respectively. In contrast, the X-built samples exhibited a higher total rise in the PLC, averaging 36 MPa and 58 MPa for the cylindrical and rectangular specimens, respectively (see Table 2). The mechanical properties indicate better isotropy, which will be discussed further in relation to the PLC region characteristics.

Stress-strain curves of a typical Z-built AMed sample is demonstrated in Figure 1. The noticed (main) PLC region is enlarged in Figure 2. The slope-up of the PLC phenomenon shows a low increase in stress, 22 MPa in 38 seconds: the trend is demonstrated, as stress versus time, in Figure 3. For comparison, stress-strain curves of a typical X-built AMed sample are demonstrated in Figure 4, and the PLC region is enlarged in Figure 5.

As for the rectangular Z-built specimens, the PLC region is much less pronounced, presenting a smaller peak, but still visible and looks divided into sub-regions, see Figure 6. When compared to the X-built specimens, one can notice that the PLC region looks continues, Figure 7. The total rise in stress during the PLC region is quite similar for the X-built, 40.65 MPa, compared to 47.55 MPa for

the Z-built.

As for the cast IN939 specimens, the PLC region shows a medium effect by size compared to the previous two samples, as presented in Figure 8 and Figure 9. Note the different features of casted IN939 (Figure 9) when compared to X-built AMed IN939 (Figure 4).

A statistical analysis of the tensile and hardness properties of AMed IN939 for both X- and Z-built orientations is presented in Table 3. The tensile properties show very low variation, with minimal standard deviation (SD) within each build direction, and the hardness values are nearly identical for both orientations. The average UTS and YS values of the X-built samples are approximately 3.4% higher

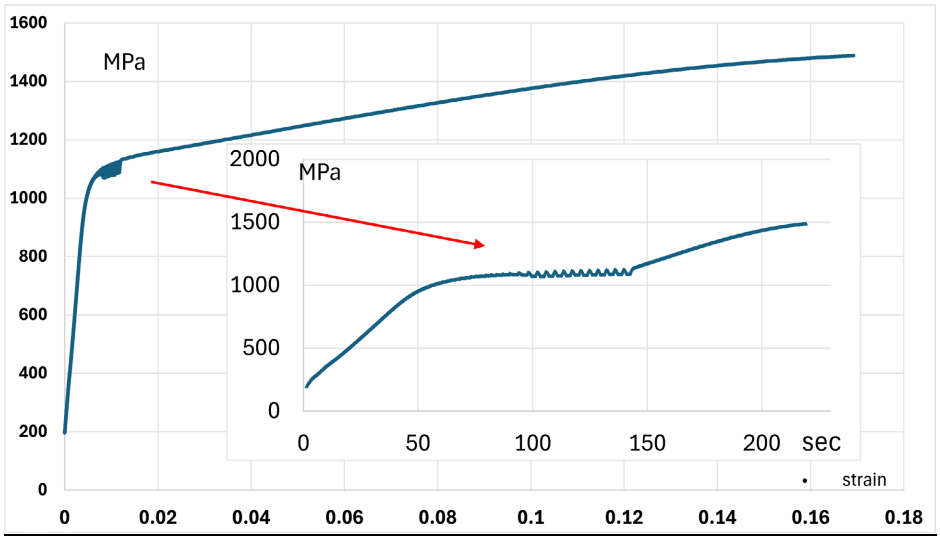

Figure 1. Stress-strain curve of the Z-bult cylindrical AMed sample. The inset presents stress vs. time graph.

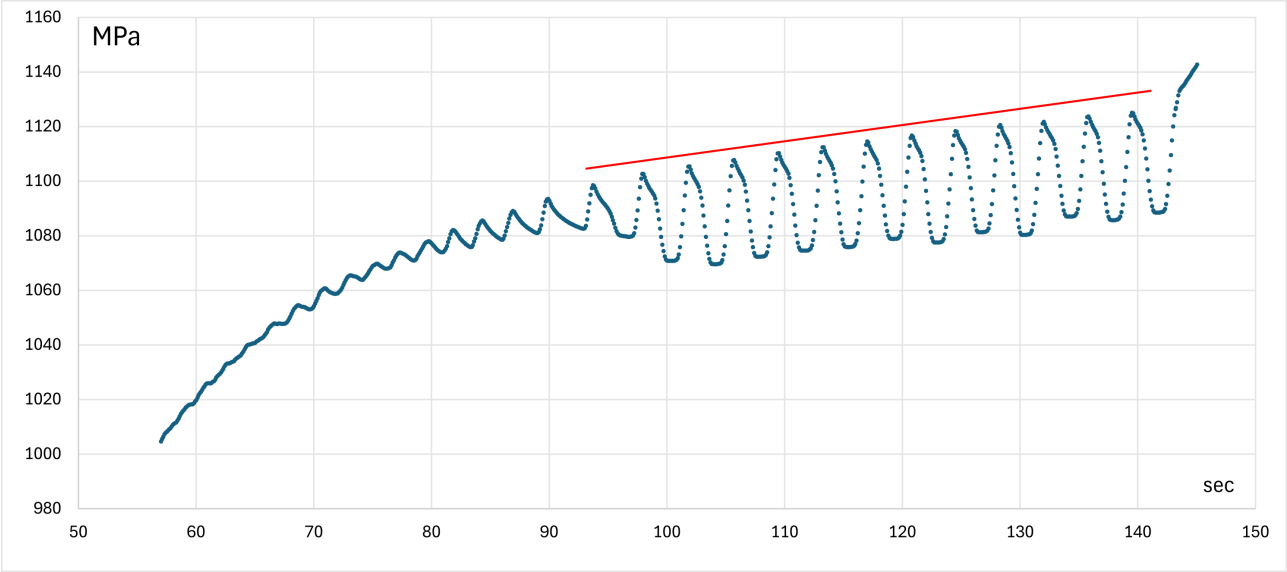

Figure 2. Stress-time curve of the PLC region in a Z-built AMed cylindrical sample. The red line represents the schematics slope calculated in Figure 3.

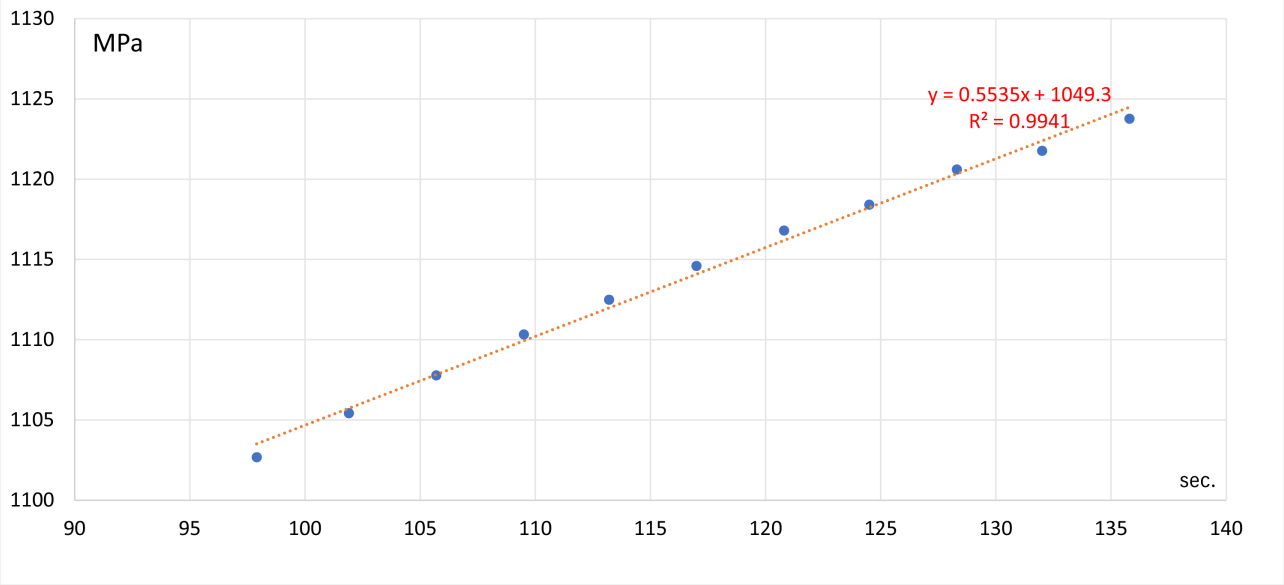

Figure 3. Stress-time curves of PLC peaks obtained in the Z-built AMed cylindrical samples.

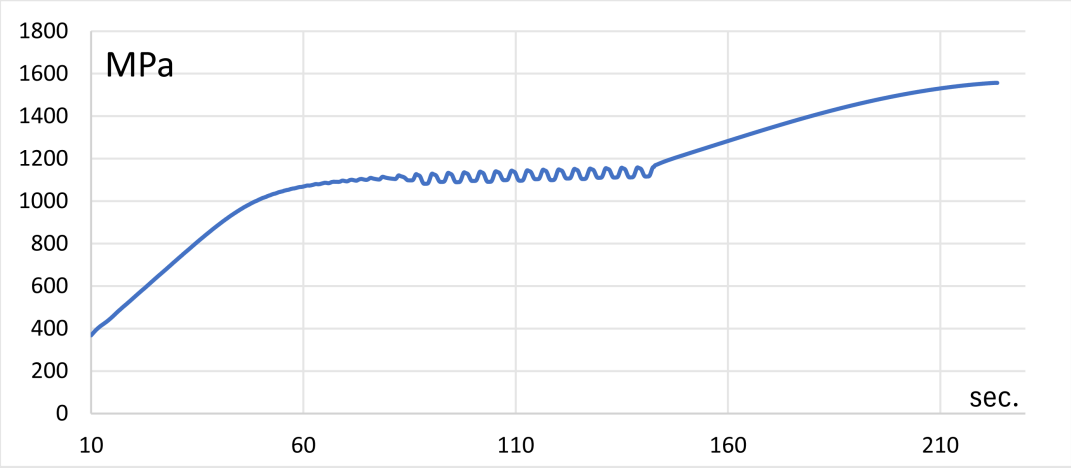

Figure 4. Stress-time curves of the X-built AMed cylindrical samples.

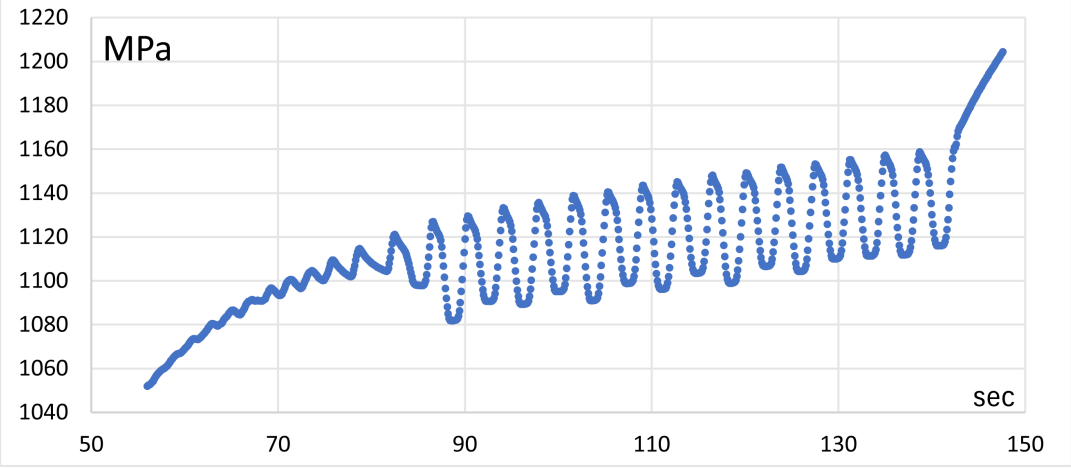

Figure 5. Stress-time curves of the PLC region of the X-built AMed cylindrical sample.

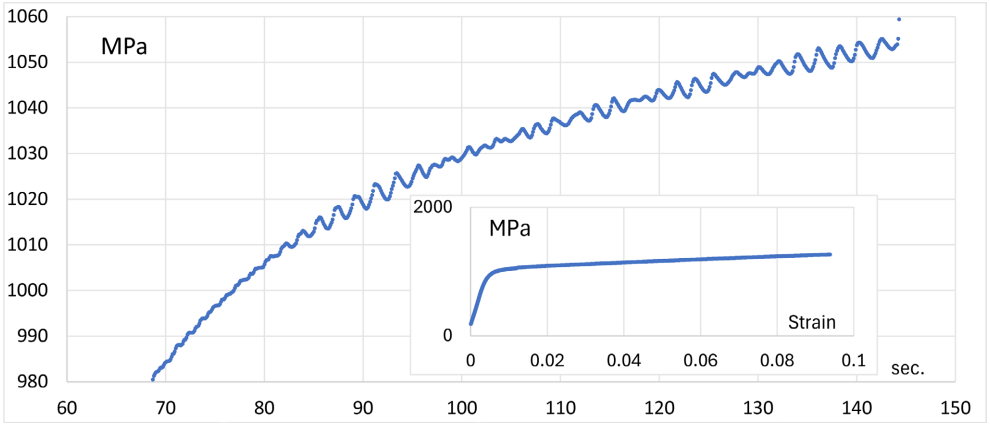

Figure 6. Stress-time (in sec.) curve of the PLC region of the Z-built AMed rectangular sample. Full stress-strain curve presented in the inset.

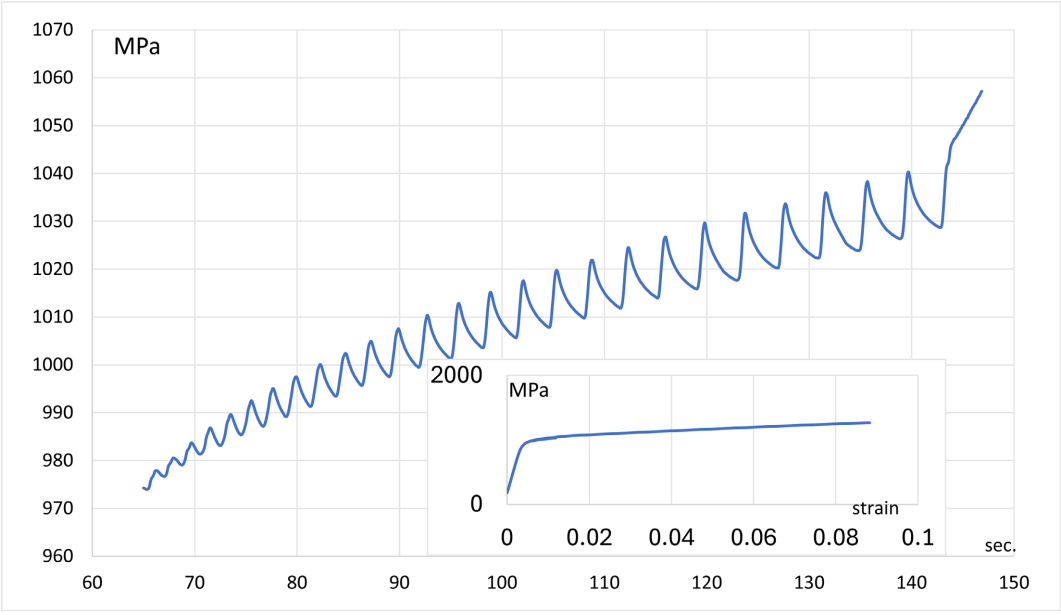

Figure 7. Stress-time curve of the PLC region of the X-built AMed rectangular sample. Full stress-strain curve presented in the inset.

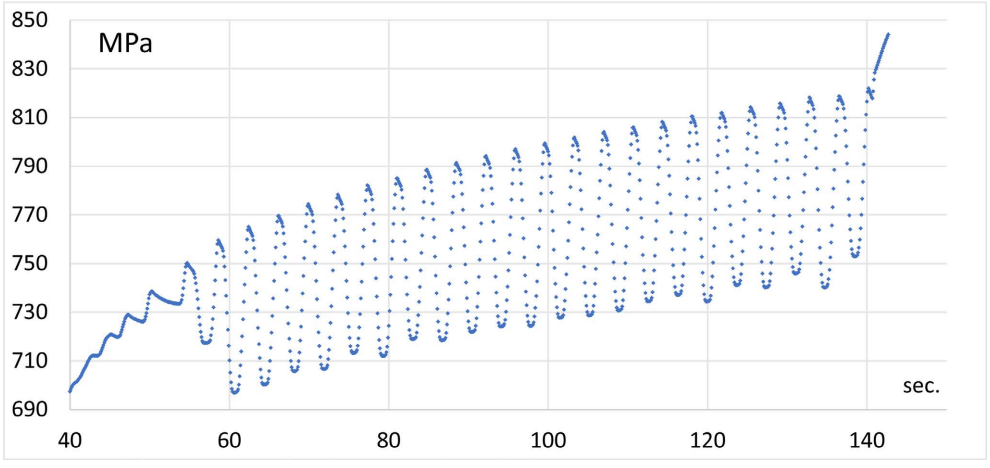

Figure 8. Enlarged view of PLC-region of the cylindrical casted IN939 from the stress-time plot.

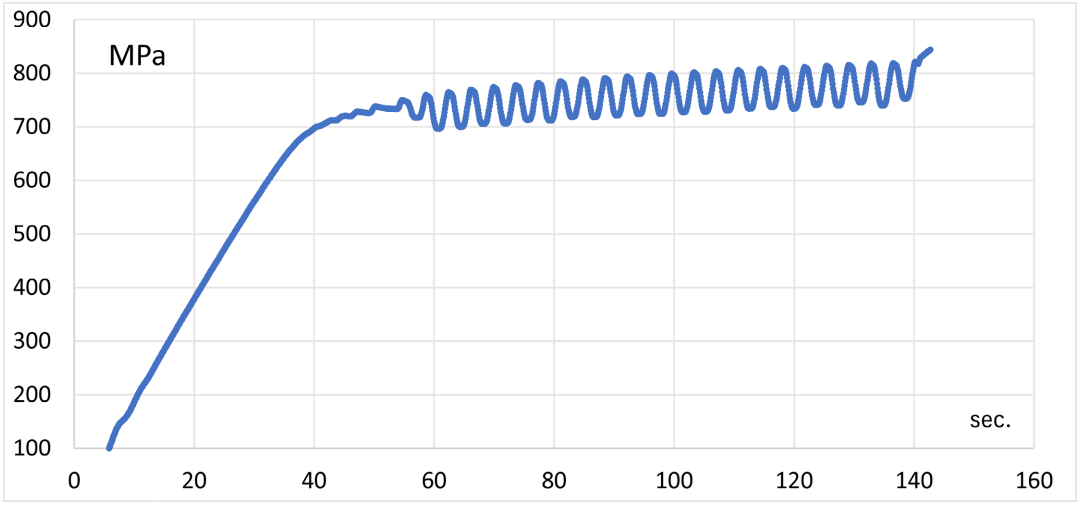

Figure 9. Stress-time curve of cylindrical casted IN939.

Table 3. Tensile and hardness data of AMed IN939 cylindrical samples and standard deviation.

VH	HRB	EL. [%]	UTS [MPa]	YS [MPa]	Modulus [GPa]	Orientation (x, z)	Sample
442	45	10	1530	1070	203	x	2.1C.X
441	45	11	1560	1100	215	x	2.2C.X
438	45	11	1550	1100	215	x	3.1C.X
447	45	10	1550	1120	221	x	3.2C.X
442	45	10.5	1547.5	1097.5	213.5	average	
0.7	0	4.7	0.7	1.6	0.2	SD [%]	
446	43	15	1500	1070	196	z	1.1C.Z
432	44	13	1510	1080	204	z	1.2C.Z
445	45	13	1490	1040	200	z	5.1C.Z
444	46	15	1490	1050	199	z	5.2C.Z
441.8	44.5	14.0	1497.5	1060.0	199.8	average	
1.3	2.5	7	.5	1.5	1.5	SD [%]	

than those of the Z-built samples, indicating minimal stress anisotropy in build strength. However, the average elongation shows a more significant difference, with the Z-built samples exhibiting 33% higher elongation than the X-built samples (14% vs. 10.5%, respectively). Grain sizes and orientations of X-built specimens show elongated grain morphology, while Z-built specimens show equiaxed grain morphology of average grain size of ASTM 4-5 [15].

4. Discussion

The PLC, as a successive deformation band, propagates after the yield to the strain-hardening region smoothly in the sample from one grip to the other during the stress-strain test is related to the energetic and hardening combination of

solute atoms and dislocations within the material due to the DSA bands [16]. These bands propagate length, inducing variations in stress and strain simultaneously. This phenomenon holds significant implications for comprehending the mechanical characteristics and performance of materials, particularly under conditions of high stress or strain. Linear stability analyses can provide useful qualitative trends as a function of the microstructural processes (slip modes, dislocation pile-up, hardness, and more). The qualitative differences in the PLC behavior of ultra-fine-grained and coarse-grained aluminum alloys in relation to the stability analysis of Hähner were discussed elsewhere [17]. There, the assumed plastic flow to occur through a thermally activated dislocation glide process is related to the following equation:

$$\dot{\varepsilon} = \nu\Omega \exp\left[\frac{\sigma_{eff} V}{kT} - \frac{G_0 + \Delta G}{kT}\right] \tag{1}$$

The strain rate presented involves the Debye frequency, (ν), in the Debye model, which provides a quantitative understanding of the heat capacity of solids, the effective stress (σ_{eff}), the activation volume (V), the constant activation enthalpy (G_0) in the absence of DSA, and the maximum increase of the free activation enthalpy (ΔG) due to DSA. The unit strain $W = \rho_m b / \sqrt{\rho_f}$ depends on the ρ_m—mobile dislocation density, ρ_f—dislocation field density, and b—the Burger's vector in the deformed zone of the sample. Applied external stress arises the ΔG due to the violation of thermodynamic equilibrium of the saluted atoms in the vicinity of the dislocation line. This unstable enthalpy arise is temporary and the thermodynamic tendency is to reduce the internal energy in the lattice simultaneously by inducing partial σ_{eff}, which acts to displace dislocations that involve more and more DSA. The accumulated plasticity in strain, in a very short time immediately after the displacement, depends on the strain rate sensitivity. The typical timetable of the PLC cycle, as derived from **Figure 2**, is as follows: 1st: the rise in stress during 1.2 sec. 2nd: drop in stress during 0.9 sec, 3rd: drop (presenting sharper slope down) during 1.0 sec, and 4th: the stage plateau during 0.6 sec. The hardening from prior plastic work by the applied stress strongly depends on the microstructure, grain size, precipitation hardening effects, and solution hardening effects. In addition, there is a characteristic rate that complies with the DSA and increases the mobility of the solute atoms (that remain behind the dislocation line and tend to diffuse through in the local deformed zone) by the local heating created by the internal frictions between the atoms and the instability of the solute atom. The metallurgical structure of Ni-base superalloys is composed of dispersed coherent γ' precipitates in a gamma solid solution matrix. The precipitation hardening of IN 939 is primarily due to the presence of the γ' phase, which acts as an intermetallic stoichiometric compound with a chemical formula based on Ni_3(Al, Ta, Nb, Ti). These precipitates act as barriers to dislocation movement when external stresses are applied to the material, causing dislocation slips to occur in the matrix surrounding the precipitates. The solid solution matrix, which is based on the FCC crystallographic lattice of Ni, accommodates all the remaining elements that

do not form the γ' phase, as well as additional elements such as W, Cr, Co, Zr, and Si, which are included in the chemical composition of the alloy. As depicted in Table 1, most of the solute elements have larger atomic radii than Ni(Al, Ti, Nb, Ta, Zr, W), some have smaller atomic radii (Si, C), while others have similar atomic radii (Cr, Co), potentially substituting Ni in the lattice matrix. The driving force for dislocation motion is primarily derived from the σ_{eff} acting on an activation volume, as expressed in Equation (1). During dislocation slip, atoms, with larger sizes near the dislocation line, lag the dislocation line, exiting from thermodynamic equilibrium. This unstable state, attributed to the change in the ΔG, tends to relax through DSA, which depends on the mobility of the solute atoms. The occurrence of DSA is observed at regular intervals, typically every 2.1 - 3.75 seconds, as illustrated in Figure 2, Figure 5, Figure 7, and Figure 8 and summarized in Table 2, for the AMed and cast samples.

In Ni-based superalloys, where strengthening depends on the precipitation hardening mechanism, the movement of dislocation lines is influenced by the σ_{eff} in the matrix phase. The presence of Ni_3(Al, Ta, Ti, Nb) precipitates impedes dislocation motion near the precipitates and not through them, causing dislocations to pile up in the matrix. Under applied stress, dislocations in the matrix might interact with solute atoms, including those from saturated precipitates-forming elements that remain in the matrix. As dislocation lines move, they increase the local energy, leading to a metastable state that prompts solute atoms to diffuse to a new position. The higher energy required for a solute atom to move to a new lattice site is due to local heating from the internal friction of atoms near the dislocation line, which can drive the solute atoms to diffuse towards a lower energy site in the lattice. A characteristic partial PDC pick-valley behavior with four distinct slopes, corresponding to different steps, is illustrated in Figure 10. The first slope reflects the increase in load required to achieve effective stresses for dislocation movement. This slope (Pseudo-modulus as attributed in Equation (1) as σ_{eff}) is 15% - 30% lower than the alloy's modulus slope but reaches the maximum local energy at the peak of the PLC cyclic behavior, see Figure 11.

As noted, dislocations lag solute atoms in less stable lattice sites, which then diffuse to more stable positions, releasing energy. The diffusion rates of larger atoms differ from those of smaller atoms, leading to two different slopes observed during DSA. According to Equation (1), once the accumulated energy is released and ΔG becomes zero, the deformation rate ($\dot{\varepsilon}$) remains constant. The schematic presentation in Figure 12 shows the three steps of the solute atoms in the matrix: before the dislocation glide, the unstable state after the dislocation slips and the reorganization of the solute atom after DSA. The explanation provided above is consistent with and supported by the analysis of Varvenne *et al.* [18] and La-Rose *et al.* [19]

Dislocation movement under stresses depends on the smoothness of the lattice and the barriers dispersed along the dislocation line path. As many barriers are present, the lattice would endure more stress. Those barriers impede the movement

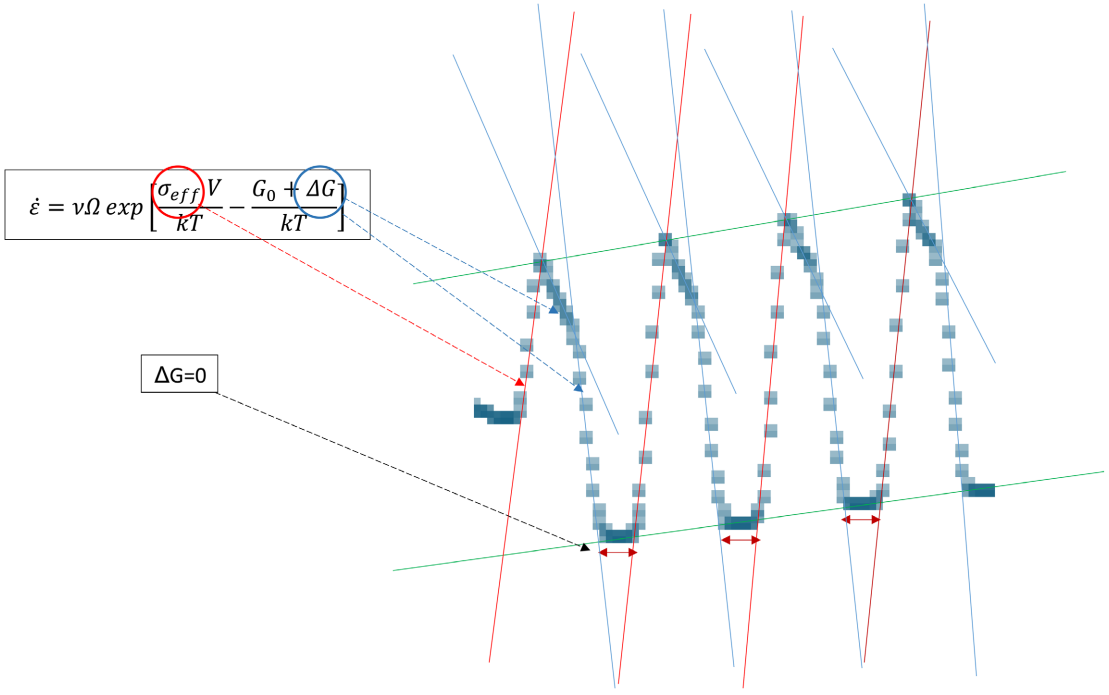

Figure 10. PLC analysis of the stress drop.

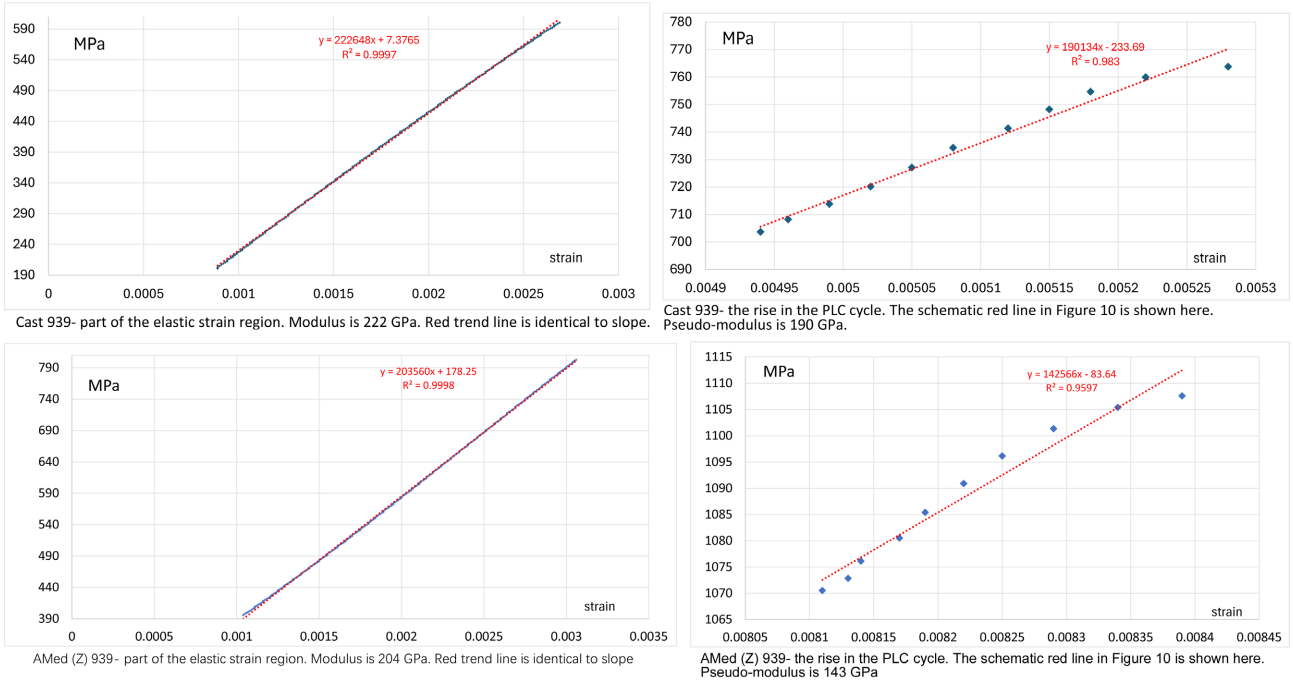

Figure 11. A comparison of the slopes of the stress-strain curves and the rise of stress in the PLC cycle for cast and AMed cylindrical samples.

of the dislocation, which prefer a lower energy path to slip, under the stress applied. The barriers could be large atoms in the lattice, coherent and semi-coherent precipitates in the lattice and dispersed phases.

Metallurgical characterization, utilizing HR-SEM, shows the characterized

primary γ' precipitates in the casted sample, Z-built AMed cylindrical sample and Z-built AMed rectangular sample, presenting different morphologies, as shown in Figures 13-15. The trinary γ' phase was practically absent in the cast sample (see Figure 13 and Figure 16), while it showed different densities in the cylindrical (CZ) and the rectangular (RZ) samples (see Figure 17 and Figure 18, respectively). The highest density can be observed in the rectangular sample, as shown in Figure 18. We suggest that the difference in the PLC serrated drop, presented in Table 2, can be attributed to the differences in the path of the dislocation line movement, affected by the characteristics of the precipitates in the samples: their amount and

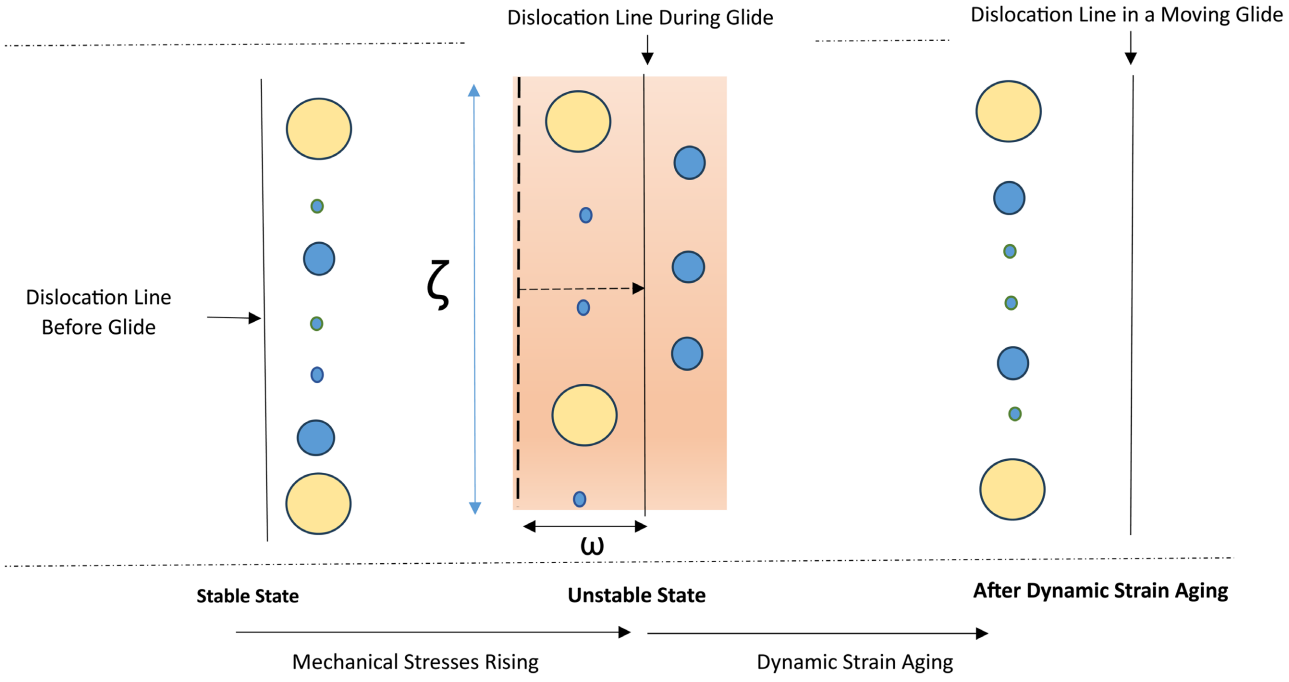

Figure 12. Schematic of the low-energy configuration of the moving dislocation through the random field of soluted atoms in the matrix. From left to right: dislocation line before glide, during glide and after DSA.

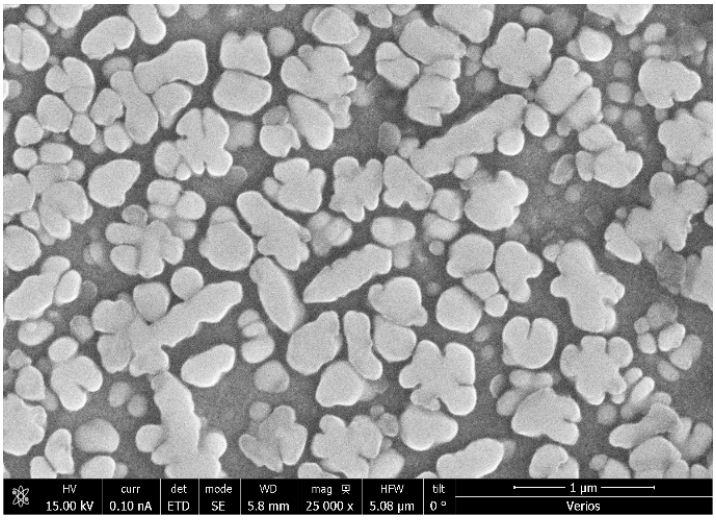

Figure 13. Cast IN939—cylindrical sample.

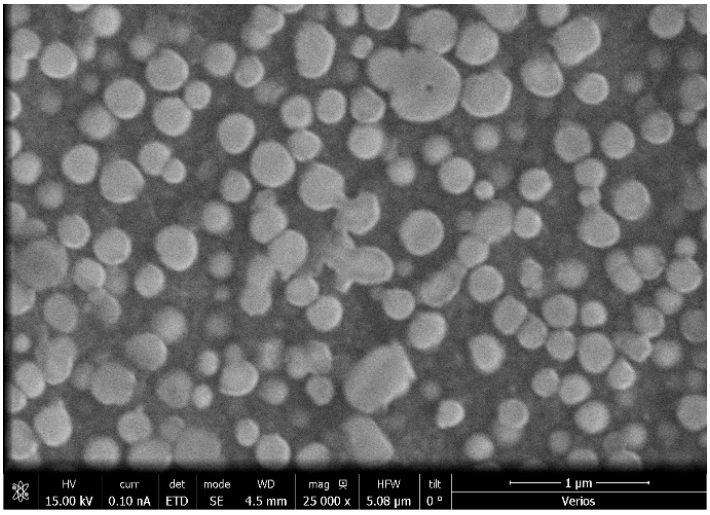

Figure 14. AMed Z-built IN939—cylindrical sample.

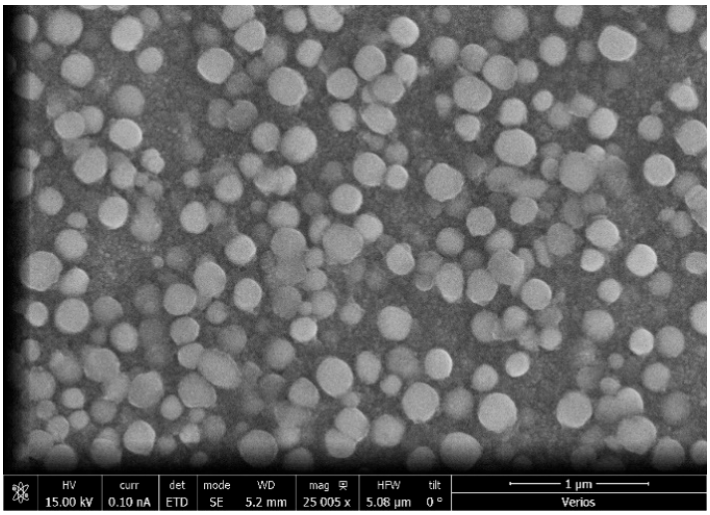

Figure 15. AMed Z-built IN939—rectangular sample.

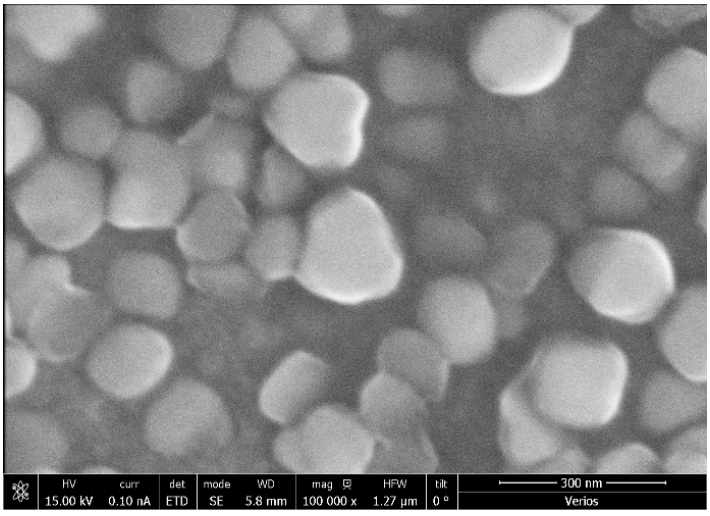

Figure 16. Cast IN939—cylindrical sample. No trinary γ' was observed.

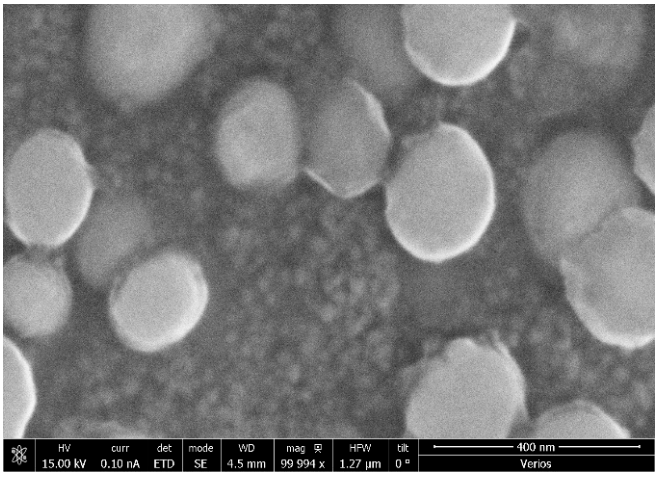

Figure 17. AMed Z-built IN939—cylindrical sample. Trinary γ' is observed among the primary γ' precipitates.

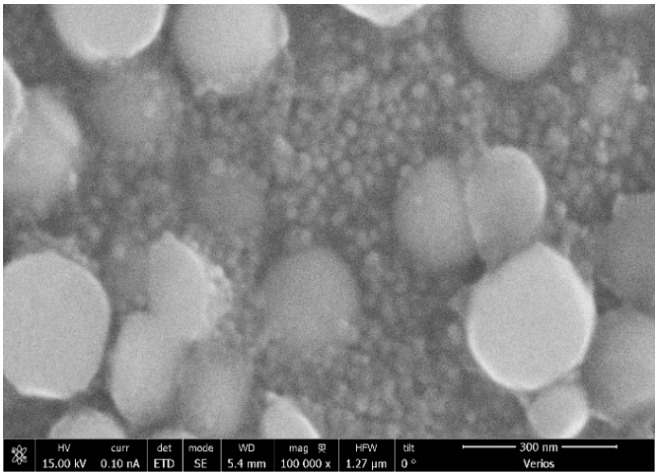

Figure 18. AMed Z-built IN939—rectangular sample. Trinary γ' at high density between the primary γ' precipitates.

the matrix zone distance between them. The largest drop, 63 - 78 [MPa], is correlated to the minimal trinary γ' amount, 36 - 40 [MPa] drop for the CZ sample is correlated to the medium trinary γ' amount, and the lowest drop (2.6 - 7 MPa) is correlated to the highest trinary γ' amount observed, as shown in **Figures 16-18**, respectively.

The recovery of the change in the free activation enthalpy, from the unstable stage to the stable stage, reduces the stresses forming the serrated drops during the stress release. The interaction of these two rates, the thermal rate and the hardening rate, determines the PLC characteristics and the DSA phenomenon observed, which is assumed here, as attributed to the different diffusion rates of divergent solute atoms.

5. Conclusions

This paper presents an investigation of the Portevin-Le Chatelier (PLC) phenomenon in AMed Inconel 939, compared to cast Inconel 939. A mechanism involving

cyclic drop-and-rise behavior is proposed, attributed to the unique morphology of the γ' precipitates in the superalloy. This mechanism aligns with the models proposed by Varvenne and La-Rose. Various characteristics of the PLC region during tensile testing were recorded and analyzed, including stress-strain behavior, amplitude, and total stress rise. HR-SEM characterization revealed distinct γ' morphologies and varying amounts of precipitates in the different samples, which were correlated to the PLC-region characteristics.

Further research is needed to deepen the understanding of the effect of PLC cycle time, particularly regarding the diffusion rates of different solute atoms in the matrix during DSA as the material transitions from unstable to stable states. Additionally, the impact of build orientation and the influence of strain rate should be explored further.

Conflicts of Interest

The authors declare no conflicts of interest regarding the publication of this paper.

References

[1] Wahl, J.B. and Harris, K. (2011) Advanced Ni Base Superalloys for Small Gas Turbines. *Canadian Metallurgical Quarterly*, **50**, 207-214. https://doi.org/10.1179/1879139511y.0000000010

[2] Sjoberg, G., Imamovic, D., Gabel, J., Cabellero, O., Brooks, J.W., *et al.* (2004) Evaluation of the IN 939 Alloy for Large Aircraft Engine Structures. *Superalloys* 2004 (*Tenth International Symposium*), Pennsylvania, 19-23 September 2004, 441-450. https://www.researchgate.net/publication/269258466 https://doi.org/10.7449/2004/superalloys_2004_441_450

[3] Shaikh, A.S. (2018) Development of a γ' Precipitation Hardening Ni-Base Superalloy for Additive Manufacturing. Chalmers University of Technology. https://hdl.handle.net/20.500.12380/255645.

[4] Moreno, D., Nahmana, Y., Nafman, O., Kam, O., Wolfman, B., Cohen, A.Y., *et al.* (2022) Mechanical Properties, Metallurgical Characteristics and Anisotropy of Additive Manufacturing of 316l. *Journal of Minerals and Materials Characterization and Engineering*, **10**, 209-223. https://doi.org/10.4236/jmmce.2022.102017

[5] Banoth, S., Li, C., Hiratsuka, Y. and Kakehi, K. (2020) The Effect of Recrystallization on Creep Properties of Alloy IN939 Fabricated by Selective Laser Melting Process. *Metals*, **10**, Article 1016. https://doi.org/10.3390/met10081016

[6] Jahangiri, M.R., Arabi, H. and Boutorabi, S.M.A. (2014) Comparison of Microstructural Stability of IN939 Superalloy with Two Different Manufacturing Routes during Long-Time Aging. *Transactions of Nonferrous Metals Society of China*, **24**, 1717-1729. https://doi.org/10.1016/s1003-6326(14)63245-3

[7] Kanagarajah, P., Brenne, F., Niendorf, T. and Maier, H.J. (2013) Inconel 939 Processed by Selective Laser Melting: Effect of Microstructure and Temperature on the Mechanical Properties under Static and Cyclic Loading. *Materials Science and Engineering: A*, **588**, 188-195. https://doi.org/10.1016/j.msea.2013.09.025

[8] Xie, J., Ma, Y., Xing, W., Zhang, L., Ou, M. and Liu, K. (2018) Heat-Affected Zone Crack Healing in IN939 Repaired Joints Using Hot Isostatic Pressing. *Welding in the World*, **62**, 471-479. https://doi.org/10.1007/s40194-018-0579-5

[9] González, M.A., Martínez, D.I., Pérez, A. and Guajardo, H. (2012) Microstructural Rejuvenation through Non-Conventional Heat Treatments of an Inconel 939 Superalloy. *MRS Proceedings*, **1372**, 89-96. https://doi.org/10.1557/opl.2012.114

[10] Marchese, G., Parizia, S., Saboori, A., Manfredi, D., Lombardi, M., Fino, P., *et al.* (2020) The Influence of the Process Parameters on the Densification and Microstructure Development of Laser Powder Bed Fused Inconel 939. *Metals*, **10**, Article 882. https://doi.org/10.3390/met10070882

[11] Le Chatelier, A. (1909) Influence du temps et de la température sur les essais au choc. *Revue de Métallurgie*, **6**, 914-917. https://doi.org/10.1051/metal/190906080914

[12] Portevin, A. and Le Chatelier, F. (1923) Sur un phénomène observé lors de l'essai de traction d'alliages en cours de transformation. *Comptes rendus de l'Académie des Sciences*, **176**, 507-510.

[13] Mogucheva, A., Saenko, M. and Kaibyshev, R. (2016) The Portevin-Le Chatelier Effect in an Al-Mg Alloy. *AIP Conference Proceedings*, Tomsk, 19-23 September 2016, Article 020156. https://doi.org/10.1063/1.4966449

[14] Tamimi, S., Andrade-Campos, A. and Pinho-da-Cruz, J. (2015) Modelling the Portevin-Le Chatelier Effects in Aluminium Alloys: A Review. *Journal of the Mechanical Behavior of Materials*, **24**, 67-78. https://doi.org/10.1515/jmbm-2015-0008

[15] ASTM International (2021) ASTM E112-13, Standard Test Methods for Determining Average Grain Size.

[16] Rowlands, B.S., Rae, C. and Galindo-Nava, E. (2023) The Portevin-Le Chatelier Effect in Nickel-Base Superalloys: Origins, Consequences and Comparison to Strain Ageing in Other Alloy Systems. *Progress in Materials Science*, **132**, Article 101038. https://doi.org/10.1016/j.pmatsci.2022.101038

[17] Joshi, S.P., Eberl, C., Cao, B., Ramesh, K.T. and Hemker, K.J. (2009) On the Occurrence of Portevin–Le Châtelier Instabilities in Ultrafine-Grained 5083 Aluminum Alloys. *Experimental Mechanics*, **49**, 207-218. https://doi.org/10.1007/s11340-008-9208-3

[18] Varvenne, C., Luque, A. and Curtin, W.A. (2016) Theory of Strengthening in FCC High Entropy Alloys. *Acta Materialia*, **118**, 164-176. https://doi.org/10.1016/j.actamat.2016.07.040

[19] LaRosa, C.R., Shih, M., Varvenne, C. and Ghazisaeidi, M. (2019) Solid Solution Strengthening Theories of High-Entropy Alloys. *Materials Characterization*, **151**, 310-317. https://doi.org/10.1016/j.matchar.2019.02.034